Journal of Materials Chemistry A

ROYAL SOCIETY OF CHEMISTRY

PAPER

View Article Online
View Journal | View Issue

Cite this: *J. Mater. Chem. A*, 2023, **11**, 9816

Sucrose-derived hard carbon wrapped with reduced graphene oxide as a high-performance anode for sodium-ion batteries†

Shengyuan Li,[a] Hong Yuan,[a] Chuanren Ye,[a] Yizhe Wang,[a] Long Wang,[b] Kun Ni*[a] and Yanwu Zhu *[ac]

Received 15th February 2023
Accepted 11th April 2023

DOI: 10.1039/d3ta00898c

rsc.li/materials-a

Further improving the performance of hard carbon anodes for sodium-ion batteries (SIBs) needs a rational design of pores, which, however, remains a challenge. Herein, hard carbon is prepared by dehydration of sucrose with 95–98% sulfuric acid, followed by annealing in NH_3/Ar at 800 °C, leading to a sample named N-HC. N-HC is dominated by mesopores, evidenced by pore volumes of 0.799 $cm^3\ g^{-1}$ measured by N_2 adsorption and 0.307 $cm^3\ g^{-1}$ by CO_2 adsorption. When N-HC is further composited with ~5 wt% graphene oxide (GO) followed by another annealing in NH_3/Ar at 800 °C, the sample (named N-HC/rGO) contains mostly ultra-micropores (<0.75 nm), showing pore volumes of 0.306 $cm^3\ g^{-1}$ measured by N_2 adsorption and 0.262 $cm^3\ g^{-1}$ by CO_2 adsorption. When being used as an anode for SIBs, N-HC/rGO shows a specific capacity of ~500 mA h g^{-1} at 0.01 A g^{-1}, which is much higher than that of N-HC (~300 mA h g^{-1}). The specific capacity of N-HC/rGO remains at 190.5 mA h g^{-1} at 1.0 A g^{-1} after 1500 cycles. The *in situ* X-ray diffraction and analysis of galvanostatic charge–discharge results indicate that the insertion of Na^+ into the carbon interlayer and filling of Na^+ in the ultra-micropores simultaneously contribute to the high plateau capacity of N-HC/rGO. When N-HC/rGO is assembled with sodium vanadium phosphate in a full coin cell, energy and power densities of 287.4 W h kg^{-1} and 4860 W kg^{-1} are demonstrated.

Introduction

Sodium-ion batteries (SIBs) have been considered as an alternative to lithium-ion batteries, due to the abundant resources and wide distribution of sodium worldwide.[1–3] Since sodium ions (Na^+) cannot intercalate into graphite spontaneously to form stable intercalated compounds, due to the weak interaction between Na^+ and graphitic layers, non-graphitic carbons such as hard carbons have attracted much attention as anodes for SIBs.[4,5] Hard carbon is composed of randomly packed carbon sheets, which cannot be fully graphitized even at a temperature of 3000 °C.[6,7] A wide range of precursors including biomass,[8] resins,[9] pitch[10] and anthracite[11] have been used to prepare hard carbons. Among them, biomass has been a focus due to the wide availability and the low cost; hard carbons made from biomass have shown an appropriate interlayer spacing of 3.6–4.2 Å and demonstrated a specific capacity of up to ~450 mA h g^{-1} as an anode for SIBs.[12,13] Corn cob,[14] shaddock peel,[15] lotus seedpod,[16] argan shell,[17] loofah sponge,[18] and rice husk[19] have been utilized to prepare hard carbons.

To further improve the performance of hard carbon anodes for SIBs, the storage mechanisms of Na^+ in hard carbon have been investigated by considering the relationship between the pore structure and ion storage. For example, Li *et al.*[20] reported a tightening of pores by depositing pyrolytic carbon on a commercial porous carbon. The pore size of the porous carbon has been reduced from a range of 0.4–2.4 nm to <0.4 nm. As a result, Na^+ is desolvated through the pores and the packing of naked Na^+ forms metallic sodium clusters in the micropores, demonstrating a discharge plateau of <0.1 V and a discharge capacity of ~400 mA h g^{-1} measured at 0.05 A g^{-1}. Xia *et al.*[21] obtained a hard carbon with uniformly distributed ultra-micropores (~0.5 nm in diameter) by heating a mixture of graphene oxide and phenolic resin at 1000 °C, which delivered a reversible capacity of 319 mA h g^{-1} at 0.02 A g^{-1} and an initial coulombic efficiency (ICE) of 71%. Youn *et al.*[22] calculated the storage of Na^+ between two graphene sheets using density functional theory. They found that the Na clusters with a size

[a]*Department of Materials Science and Engineering, School of Chemistry and Materials Science, University of Science and Technology of China, Hefei, Anhui 230026, P. R. China. E-mail: zhuyanwu@ustc.edu.cn; nikun@ustc.edu.cn*

[b]*Fu'an Guolong Nano Material, Co. Ltd, Ningde, Fujian 352000, P. R. China*

[c]*Key Laboratory of Precision and Intelligent Chemistry, University of Science and Technology of China, Hefei, Anhui 230026, China*

† Electronic supplementary information (ESI) available: DSC results, XRD fitting and EDS elemental mappings of samples. XPS survey spectra and S 2p of N-HC and N-HC/rGO. Electrochemical performance of N-rGO, N-HC, N-HC/rGO and NVP electrodes. *In situ* XRD result of N-HC/rGO. SEM images of NVP before and after cycling. The table of XPS data and electrochemical performance compared with other hard carbon electrodes. See DOI: https://doi.org/10.1039/d3ta00898c

smaller than 1.87 nm are energetically stable in the micropores between graphene layers, showing a quasi-metallic feature and a positive insertion potential relative to Na/Na^+. In previously reported preparations, annealing the precursors at different temperatures[14–19] or using templates (*e.g.*, particles of MgO and SiO_2 (ref. 23 and 24)) has been commonly utilized to tune the pore structure of hard carbons. However, hard carbons made at low annealing temperatures (<1100 °C) usually have a wide pore distribution and a low graphitization degree,[12] leading to low electrical conductivity and poor electrochemical stability.[25] A higher temperature annealing may improve the graphitization degree, but typically results in the collapse of pores and thus a reduced specific surface area (SSA) and pore volume, deteriorating the Na^+ storage.[26] The introduction and removal of templates would also bring about extra complexity to the preparation. Therefore, a straightforward yet feasible way to prepare hard carbons with a tunable pore structure and good electric conductivity is desired.

In this work, raw hard carbon is prepared by dehydration of sucrose with 95–98% sulfuric acid. Nitrogen-doped hard carbon (N-HC) is prepared by annealing raw hard carbon in NH_3/Ar at 800 °C for 6 h. N-HC has an SSA of 1535.9 $m^2\ g^{-1}$ and a pore volume of 0.799 $cm^3\ g^{-1}$, dominated by micro- or meso-pores (>0.75 nm). By compositing with graphene oxide and then annealing in NH_3/Ar at 800 °C again, the newly obtained sample (N-HC/rGO) is dominated by ultra-micropores (0.3–0.75 nm). As an anode for SIBs, N-HC/rGO demonstrated an impressive specific capacity of ~500 mA h g^{-1} at 0.01 A g^{-1}, compared to ~300 mA h g^{-1} of N-HC at 0.01 A g^{-1}. Long cycling testing of the N-HC/rGO anode at 1.0 A g^{-1} shows a capacity retention of 80.7% after 1500 cycles. Based on *in situ* X-ray diffraction (XRD) and galvanostatic charge–discharge (GCD) measurements, the Na^+ storage mechanism in N-HC/rGO is considered as the combination of adsorption, intercalation and micropore filling. An N-HC/rGO//$Na_3V_2(PO_4)_3$ (NVP) full-cell device exhibits specific energy and power densities of 287.4 W h kg^{-1} and 4860 W kg^{-1}.

Experimental

Preparation of N-HC and N-rGO samples

5.0 g sucrose (Sinopharm Chemical Reagent Co., Ltd) was put into a 200 mL beaker with 1 mL deionized water added dropwise. Then 9 mL sulfuric acid (H_2SO_4, 95–98% wt%, Sinopharm Chemical Reagent Co., Ltd) was added dropwise into the beaker under magnetic stirring. The white sucrose turns yellow at first and then gradually turns brown, followed by forming a black foam. The black foam was collected and washed with water till neutral; the yield is ~73% due to the incomplete dehydration reaction. The washed sample was freeze-dried and annealed at 800 °C for 6 h with a heating rate of 5 °C min^{-1} in NH_3/Ar (v/v = 1 : 1), to form nitrogen-doped hard carbon (N-HC). In addition, nitrogen-doped reduced graphene oxide (N-rGO) was obtained using graphene oxide (GO) as the raw material and annealed at 800 °C for 3 h with a heating rate of 5 °C min^{-1} in NH_3/Ar (v/v = 1 : 1).

Preparation of N-HC/rGO composites

0.77 g N-HC was put into 200 mL of ethanol, and 10 mL of GO suspension (in water, 3.85 mg mL^{-1}) was put into 200 mL of deionized water. The samples were under ultrasonication for 30 min to form homogeneous suspensions. Then, the N-HC suspension was added dropwise into the GO suspension under magnetic stirring to form N-HC/GO mixed suspension. The obtained N-HC/GO suspension mixture was freeze-dried and annealed at 800 °C for 3 h with a heating rate of 5 °C min^{-1} in an NH_3/Ar (v/v = 1 : 1) atmosphere, to form the N-HC/rGO sample.

Characterization methods

The morphology of samples was characterized by scanning electron microscopy (SEM, Hitachi, SU8200, Japan) and high-resolution transmission electron microscopy (HR-TEM, JEOL-2100F, Japan). The samples were evaluated by Raman spectroscopy (LabRAM, RM3000, Renishaw, UK, 532 nm laser) and Fourier-transform infrared (FTIR, attenuated total reflection mode, Thermo Nicolet nexus-470, US) spectroscopy. Differential scanning calorimetry (DSC) was conducted using a DSC Q2000 (TA Corporation, USA) from 30 °C to 810 °C in an oxygen atmosphere at a heating rate of 10 °C min^{-1}. XRD with Cu Kα radiation (λ = 1.5418 Å, tube voltage 40 kV, tube current 30 mA, Rigaku SmartLab, Japan). The chemical composition was characterized by X-ray photoelectron spectroscopy (XPS) on a Thermo ESCALAB 250 (US) with Al Kα radiation ($h\nu$ = 1486.6 eV), and all spectra were calibrated to the binding energy of C=C bonds (284.6 eV). N_2 adsorption/desorption and CO_2 adsorption isotherms were recorded with a Quantachrome Autosorb-IQ apparatus (USA).

Fabrication of half-cell and N-HC/rGO//NVP devices

For the fabrication of anodes, 80 wt% active material (N-rGO, N-HC or N-HC/rGO) was mixed with 20 wt% polyvinyl fluoride (PVDF) and dispersed in *N*-methyl-2-pyrrolidone (NMP) to form a slurry. The slurry was spread and pressed on copper foil and dried at 80 °C for 12 h in a vacuum. Active material with a mass loading of 1.0–1.5 mg cm^{-2} was punched into round electrodes with a diameter of 10 mm. 2032-type coin half cells were assembled in an Ar-filled glove box (H_2O and O_2 concentrations below 1.0 ppm), using sodium foil simultaneously as the reference and counter electrode, 1.0 M $NaPF_6$ in diethylene glycol dimethyl ether (DEGDME) as the electrolyte, and a Celgard 2400 porous polypropylene membrane as the separator.

N-HC/rGO//NVP full cells

The full cells were assembled in coin cells by using N-HC/rGO as an anode (galvanostatically charged–discharged for 5 cycles and ending in a sodiated state at 0.001 V under a low current density of 0.01 A g^{-1}) and a commercial $Na_3V_2(PO_4)_3$ (NVP, Canrd) cathode in 1.0 M $NaPF_6$ in a 1 : 1 (v/v) mixture of ethylene carbonate (EC) and diethyl carbonate (DEC) with 5% fluoroethylene carbonate (FEC) as the electrolyte. For the fabrication of cathodes, 80 wt% NVP powder and 20 wt% PVDF were mixed

and then dispersed in NMP to form a slurry. The slurry was spread and pressed on aluminum foil and dried at 80 °C for 12 h in a vacuum. The mass ratio of N-HC/rGO and NVP is 1 : 3 according to N/P = 1–1.2. The voltage window of 0.001–4.0 V was taken to avoid the oxidative decomposition of electrolytes and achieve high energy density.

Electrochemical measurements

Cyclic voltammetry (CV) at various scan rates and electrochemical impedance spectroscopy (EIS) measurements in the frequency range from 100 kHz to 0.01 Hz were performed on a CHI 760E electrochemical workstation (CH Instruments, Inc., Shanghai). Galvanostatic charge–discharge measurements at various current densities and cycle stability tests for half and full cells were conducted on a Land CT 2001A battery test system. The weight (anode or cathode) was based on the active materials, excluding PVDF.

Results and discussion

Morphological and structural characterization

Fig. 1a schematically illustrates the preparation of N-HC and N-HC/rGO starting from sucrose, sulfuric acid and graphene oxide. In brief, the dehydration reaction of sucrose with 95–98% sulfuric acid was taken to prepare an intermediate raw carbon (HC raw), which was annealed at 800 °C in NH_3/Ar to form N-HC. N-HC/rGO was obtained from a mixture of N-HC suspension in ethanol and graphene oxide aqueous suspension, followed by freeze-drying and another thermal annealing treatment at 800 °C in NH_3/Ar for 3 hours. The mass ratio of N-HC and GO is 20 : 1. Scanning electron microscopy (SEM) and transmission electron microscopy (TEM) images in Fig. 1b and c show that N-HC is porous and fragmented. The high-resolution TEM (HRTEM) image in Fig. 1d shows randomly distributed, curved layers of N-HC; the interlayer spacing is estimated to be 0.408 nm. The selected area electron diffraction (SAED) pattern confirms the amorphous feature of N-HC. The SEM (Fig. 1e) and TEM (Fig. 1f) images of N-HC/rGO show the presence of randomly distributed rGO sheets and anchoring of N-HC on rGO sheets;[27] the observation of a smaller layer spacing of ~0.361 nm in Fig. 1g could be related to rGO. Differential scanning calorimetry (DSC) testing performed from 30 to 810 °C in oxygen (Fig. S1†) shows that N-HC or N-rGO has one exothermic peak located at 640.2 °C or 597.8 °C, respectively, while a broad exothermic peak located at 601.9 °C is observed from N-HC/rGO. The difference might indicate that N-HC and rGO are chemically bonded.[28]

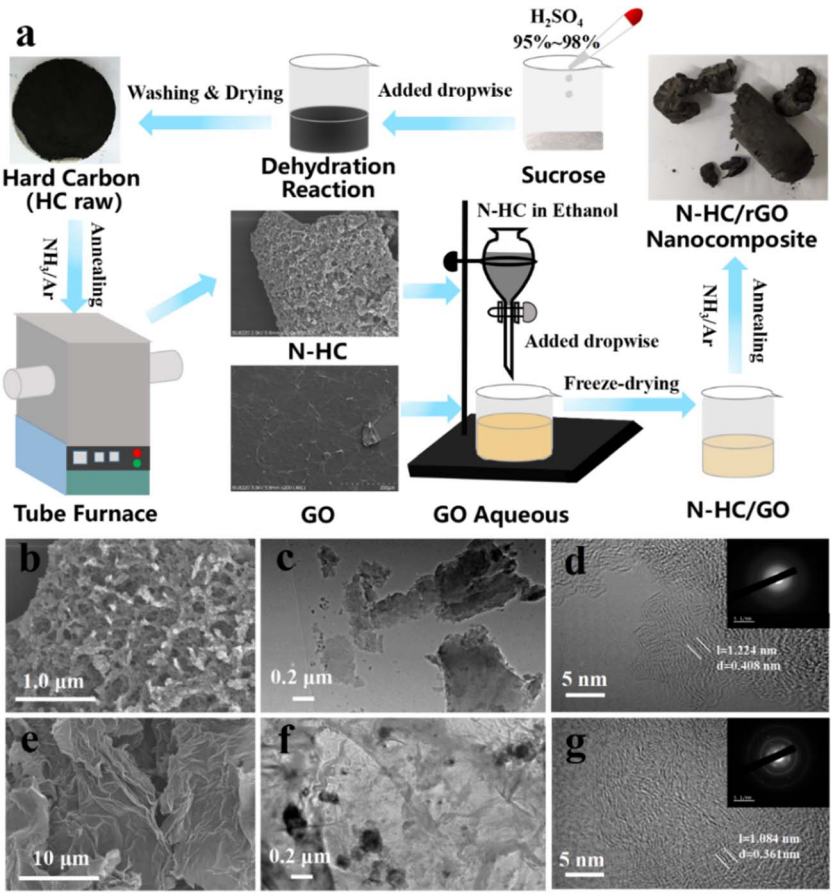

Fig. 1 (a) Schematic illustration of the preparation of N-HC and N-HC/rGO. (b) SEM, (c) TEM and (d) HRTEM (inset: SAED pattern) images of N-HC and (e) SEM, (f) TEM and (g) HRTEM (inset: SAED pattern) images of N-HC/rGO.

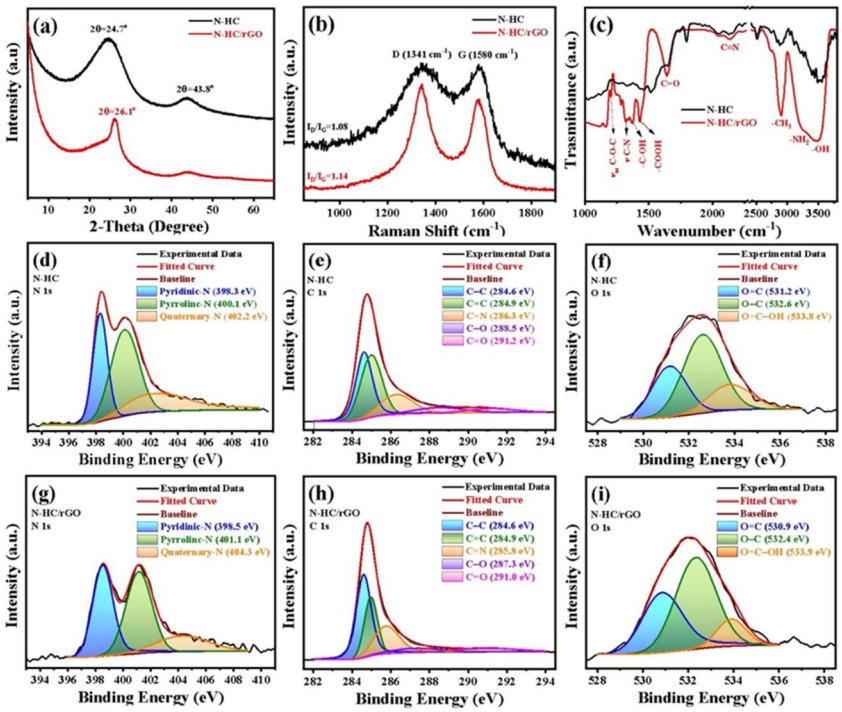

Fig. 2 (a) XRD patterns, (b) Raman spectra and (c) FTIR spectra of N-HC and N-HC/rGO. XPS (d) N 1s, (e) C 1s and (f) O 1s spectra and convolutions of N-HC. XPS (g) N 1s, (h) C 1s and (i) O 1s spectra and convolutions of N-HC/rGO.

Fig. 2a shows that the XRD pattern of N-HC has two broad peaks at $2\theta = 24.7°$ (0.360 nm) and $2\theta = 43.8°$ (0.207 nm). In contrast, N-HC/rGO has a sharper peak at $2\theta = 26.1°$ (0.341 nm), attributed to the presence of rGO.[29] Profile-fitting of (002) peaks in Fig. S2a and b† further shows that, compared with N-HC, N-HC/rGO has a reduced interlayer spacing; the peak at 26.1° contributes to 63.3% of all layer distances in N-HC/rGO, lower than 84.7% for the peak at 24.7° of N-HC. It was reported that a minimum interlayer distance of 0.37 nm in carbon is required for Na^+ diffusion.[15,29] The Raman spectra of N-HC and N-HC/rGO are shown in Fig. 2b. The higher I_D/I_G ratio of N-HC/rGO (1.14 *vs.* 1.08 of N-HC) indicates more defects in N-HC/rGO. From Fourier transform infrared (FTIR) analysis shown in Fig. 2c, residual oxygen-containing functional groups (*e.g.*, –OH, ~3483.6 cm^{-1}; –COOH, ~1430.8 cm^{-1}; –COH, ~1370.2 cm^{-1}) have been identified. The presence of nitrogen-containing groups (–N–H, ~3245 cm^{-1}; –C≡N, ~2136 cm^{-1}; –C–N, ~1315 cm^{-1}) indicates the successful doping of nitrogen atoms in N-HC and N-HC/rGO,[30,31] also confirmed by EDS elemental mapping (Fig. S3†) and X-ray photoelectron spectroscopy (XPS, Fig. 2d and g and S4a†). The XPS N 1s spectra of N-HC and N-HC/rGO can be deconvoluted into three peaks ascribed to pyridinic-N (398.5 eV), pyrrolic-N (401.1 eV) and graphitic-N (404.3 eV).[32] Compared with N-HC (72.2%), N-HC/rGO has a higher content (83.7%) of pyridinic-N and pyrrolic-N, as can be obtained by comparing Fig. 2d and g (more XPS convolution data in Table S1†). From XPS C 1s, O 1s and N 1s spectra shown in Fig. 2d–i, we find that N-HC/rGO has lower C 1s and O 1s bonding energies in C–O bonds yet higher N 1s bonding energy in C–N bonds, compared to those in N-HC. The result might be related to the electron transfer from N-HC to rGO.[29,30,32] No sulfur was detected (Fig. S4b and c†).

The pore structures of N-HC and N-HC/rGO were characterized by N_2 adsorption/desorption and CO_2 adsorption. Fig. 3a and b show the calculated SSA depending on the pore width. For N-HC, an SSA of 1535.9 $m^2\ g^{-1}$ is obtained from N_2 adsorption and 881.6 $m^2\ g^{-1}$ from CO_2 adsorption; the SSA of N-HC/rGO measured from N_2 adsorption reduces to 615.1 $m^2\ g^{-1}$ but that obtained from CO_2 adsorption increases to 973.8 $m^2\ g^{-1}$. Specifically, from Fig. 3b we can see a sharp increase of the SSA attributed to ultra-micropores, which are defined with a pore width of <0.75 nm. With a pore volume of 0.799 $cm^3\ g^{-1}$ measured by N_2 adsorption/desorption, N-HC has rich micro- or meso-pores with widths in the range of 0.75 to 3.75 nm with

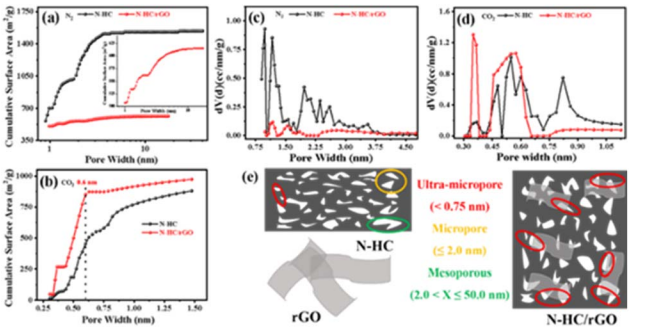

Fig. 3 (a) SSA is calculated from (a) N_2 or (b) CO_2 adsorption and corresponding pore width distributions measured by (c) N_2 adsorption or (d) CO_2 adsorption. (e) Schematic illustration of the pore size change of N-HC by the wrapping of rGO.

peaks at 0.98, 1.12 and 1.96 nm, as can be seen in Fig. 3c. In contrast, the pore volume of N-HC/rGO measured by N_2 adsorption/desorption is reduced to 0.306 $cm^3\ g^{-1}$ with two lower peaks observed at 1.17 and 1.55 nm. The CO_2 adsorption measurement shows that N-HC/rGO has an ultra-micropore volume of 0.215 $cm^3\ g^{-1}$, much higher than that of 0.151 $cm^3\ g^{-1}$ for N-HC, as shown in Fig. 3d. The comparison indicates that the composition of N-HC with rGO has reduced the volume of mesopores but increased the fraction of ultra-micropores. To further investigate the effect of second annealing on the pore structure, control samples N-HC-3h (obtained by the second annealing of N-HC in NH_3/Ar for 3 h) and N-rGO (obtained by the annealing of GO in NH_3/Ar for 3 h) were also characterized by N_2 gas adsorption. As shown in Fig. S5a–c,† the SSA and pore volume of N-HC-3h measured by N_2 adsorption are lower than those of N-HC and N-HC/rGO. More importantly, Fig. S5d–f† reveal that the specific surface area and pore volume from CO_2 measurement are 461.4 $m^2\ g^{-1}$ and 0.166 $cm^3\ g^{-1}$ for N-HC-3h, much lower than the SSA and pore volume of N-HC. As shown in Fig. S6,† the SSA of N-rGO measured by N_2 adsorption was 24.2 $m^2\ g^{-1}$ and the pore volume was 0.044 $cm^3\ g^{-1}$ with size mainly between 3.0 and 20.0 nm.

Compared with N-HC (0.151 $cm^3\ g^{-1}$) and N-HC-3h (0.129 $cm^3\ g^{-1}$), the ultra-micropore (<0.75 nm) volume of N-HC/rGO is 0.215 $cm^3\ g^{-1}$, suggesting the necessity of GO in terms of ultra-micropore tuning. Such a pore size tuning is schematically illustrated in Fig. 3e, in which some of the micro- or meso-pores in N-HC may be partially covered by rGO, resulting in the decrease of such pores and thus a relative increase in the volume of ultra-micropores.

Electrochemical characterization

Fig. 4a shows the cyclic voltammetry (CV) curves of N-HC and N-HC/rGO anodes for SIBs recorded at 0.1 mV s^{-1} in the first cycle, in which both samples have a pair of sharp oxidation reduction peaks below 0.1 V, attributed to the insertion/desertion of Na^+ into/from hard carbon.[21] The larger area of CV curves of N-HC/rGO indicates a higher Na^+ storage capacity compared to N-HC.[33] The additional pair of oxidation–reduction peaks at 0.8/0.6 V for N-HC/rGO electrodes may be attributed to the presence of N-doped rGO in N-HC/rGO, because a similar pair of peaks have been observed from N-rGO, as shown in the CV curves in Fig. S7a.† The N-rGO anode shows a capacity of ~500 mA h g^{-1} at 0.1 A g^{-1} (~200 mA h g^{-1} at 1.0 A g^{-1}, shown in Fig. S7c†) while poor cycling stability, as can be seen from Fig. S7b.† Due to the relatively small amount of rGO in the N-NC/rGO sample (~5 wt%), the capacity of N-NC/rGO should not be mainly provided by the rGO component. Fig. 4b shows the electrochemical impedance spectroscopy (EIS) results of N-HC and N-

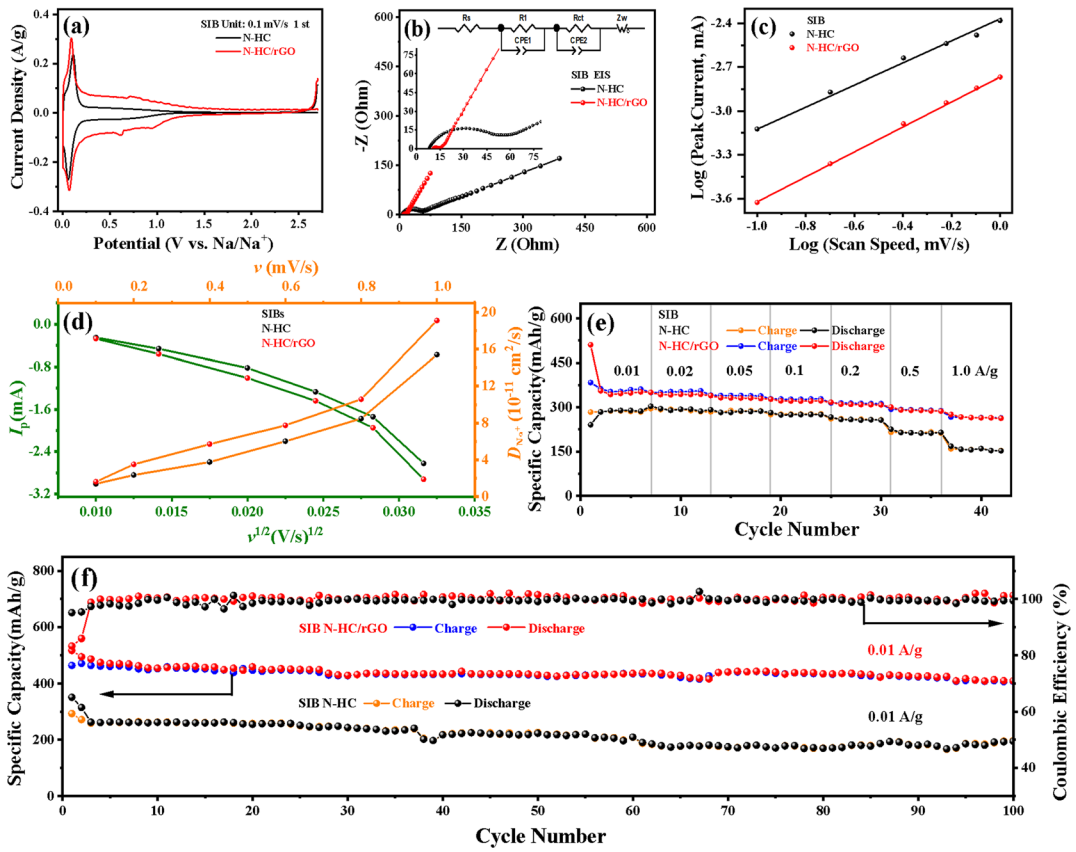

Fig. 4 Electrochemical performance evaluation of N-HC and N-HC/rGO anodes for SIBs. (a) CV curves obtained at 0.1 mV s^{-1} in the first cycle; (b) Nyquist plots (inset images: equivalent circuit diagram); (c) relationship of log(v) *vs.* log(i) for N-HC and N-HC/rGO; (d) diffusion coefficient of Na^+ depending on scan rates, calculated from the I_p–$v^{1/2}$ curves of N-HC and N-HC/rGO electrodes; (e) rate capability measured from 0.01 to 1.0 A g^{-1}; (f) cycling performance tested at 0.01 A g^{-1}.

HC/rGO electrodes. The fitting of the equivalent circuit diagram gives a charge transfer resistance (R_{ct}) value of 57.3 Ω or 6.7 Ω, for N-HC or N-HC/rGO, respectively, suggesting that N-HC/rGO has a better electrical conductivity.

The CV curves of N-HC and N-HC/rGO recorded at different scan rates are shown in Fig. S8a and b,† from which we can see that N-HC/rGO has smaller changes of ohmic polarization with the increase of the scan rate, compared with N-HC. Using data of the scan rate (v) and peak current (i), the slope b of $\log(v)$ *vs.* $\log(i)$ curves can be calculated following the equation $i = av^b$.[21,25] As shown in Fig. 4c, $b = 0.86$ is obtained for the N-HC/rGO electrode, while $b = 0.72$ for N-HC, suggesting a more surface capacitive-controlled process for the N-HC/rGO electrode.[21,34] Based on I_p–$v^{1/2}$ curves, the diffusion coefficient of Na^+ (D_{Na^+}) has been estimated according to the relationship, $I_p = 2.69 \times 10^5 An^{3/2} C_0 D_{Na^+}{}^{1/2} v^{1/2}$,[34] where A, n and C_0 stand for the geometric area of electrodes, the number of electrons involved in the redox reaction and the molar concentration of Na^+ in electrode. As shown in Fig. 4d, the D_{Na^+} values of N-HC (1.4×10^{-11} cm^2 s^{-1}) and N-HC/rGO (1.63×10^{-11} cm^2 s^{-1}) obtained at 0.1 mV s^{-1} are very close, as the time is long enough for Na^+ to diffuse at 0.1 mV s^{-1}. With the increase in the scan rate, however, the diffusion coefficient of Na^+ in N-HC/rGO increases faster than that of N-HC; values of 1.54×10^{-10} cm^2 s^{-1} and 1.91×10^{-10} cm^2 s^{-1} at 1.0 mV s^{-1} for N-HC and N-HC/rGO are close to the reported values from hard carbons.[34] The higher diffusion rates of N-HC/rGO may be attributed to more ultra-micropores (<0.75 nm) in N-HC/rGO, so that de-solvated Na^+ can quickly transport through the micropores.[20]

As a result of the faster ionic diffusion, the N-HC/rGO electrode possesses a better rate performance than the N-HC electrode, as shown in Fig. 4e. Specifically, the capacity of the N-HC/rGO electrode is 510.5 mA h g^{-1} at 0.01 A g^{-1}, which remains at 266.8 mA h g^{-1} at 1.0 A g^{-1}. From the cycling results shown in Fig. 4f, we can see that the capacity retention (relative to that in the 2nd cycle, all the same below) of N-HC and N-HC/rGO electrodes is 56.7% and 78.7%, respectively, after 100 cycles tested at 0.01 A g^{-1}. At 0.1 A g^{-1} (Fig. S8c†), the capacity retention is 84% for N-HC/rGO after 500 cycles while that of N-HC is 51.2%. When the discharge current density is increased to 1.0 A g^{-1} (Fig. S8d†), the capacity retention of HC/rGO is still about 85% after 1500 cycles, whereas that of the N-HC anode is less than 50%. In addition, the ICE of N-HC/rGO (84.7%) is also higher than that of N-HC (75.1%) at 0.01 A g^{-1}. In contrast, the cycling test of the N-HC-3h electrode performed at 0.1 and 1.0 A g^{-1}, as shown in Fig. S9,† indicates the first charge or discharge capacity of 219.6 or 354.2 mA h g^{-1} at 0.1 A g^{-1}, respectively. The specific capacity of N-HC-3h remains at 189.4 mA h g^{-1} at 0.1 A g^{-1} after 38 cycles, and 147.7 mA h g^{-1} at 1.0 A g^{-1} after 115 cycles, lower than those of N-HC and N-HC/rGO.

Clearly, we can see the N-HC/rGO anode has better electrochemical performance compared to N-HC or N-HC-3h. The high specific capacity of N-HC/rGO may be due to more accessible ultra-micropores, which improve the de-solvation and thus the diffusion of Na^+.[20,35] The high electronic conductivity of rGO may enhance the conductivity of the N-HC/rGO electrode and improve the mechanical stability of N-HC during cycling as well.[36–38] In addition, pyridinic-N and pyrrolic-N shall provide extra active sites for Na^+ adsorption in N-HC/rGO. The specific capacity and rate performance as well as cycling performance of N-HC/rGO are also better than those of most hard carbons obtained from various precursors, as shown in Table S2.†

To reveal the storage mechanism of Na^+, we performed *in situ* XRD. The peak at 26.1° of rGO is very close to the peak of N-HC, so the XRD signal of N-HC/rGO was not distinguished for different voltages as shown in Fig. S10.† The *in situ* XRD results of N-HC corresponding to the first discharge/charge cycle at 0.1 A g^{-1} are shown in Fig. 5a, from which we can see that the new peak at $2\theta = 22.32°$ shifts to $2\theta = 22.04°$ ($\Delta 2\theta \approx 0.3°$) at a discharge voltage of 0.001 V. The shifting to large angles indicates that the interlayer spacing is expanded, due to Na^+ insertion.[12] When N-HC is charged to 2.7 V, the peak of $2\theta = 22.04°$ shifts to $2\theta = 22.18°$ instead of $2\theta = 22.32°$, suggesting that Na^+ is not fully removed from the N-HC interlayer.

The origin of capacity has also been analyzed by taking the GCD measurement of N-HC and N-HC/rGO in the first two cycles at 0.01 A g^{-1}, as shown in Fig. 5b. The total discharge capacities of N-HC or N-HC/rGO in the 2nd cycle are estimated to be 267.4 mA h g^{-1} or 495.6 mA h g^{-1}, respectively. For N-HC, the slope region capacity (>0.1 V) and plateau region capacity (<0.1 V) are 117.8 and 149.6 mA h g^{-1}, which are increased to 216.2 and 279.4 mA h g^{-1} for N-HC/rGO. The capacity increase in the slope region may be due to more adsorption of Na^+ on the structural defects introduced by pyridinic-N and pyrrolic-N doping. In addition, the presence of N-rGO in N-HC/rGO also provided a surface for Na^+ adsorption and helps to improve the slope region capacity. It has been reported that the ultra-micropores can screen out solvated Na^+ and enable the formation of sodium clusters to produce the plateau, thus increasing the plateau capacity.[20] Since N-HC/rGO has more ultra-micropores (<0.75 nm), the increase in the capacity of the plateau region may indicate that the Na^+ storage behavior in N-HC/rGO is closely related to the pore-filling mechanism, consistent with the results reported in the literature.[2,7,11,12,20,22]

With the better electrochemical performance, N-HC/rGO has been used as an anode to assemble a full cell with commercial sodium vanadium phosphate ($Na_3V_2(PO_4)_3$, NVP) as the cathode. The moderate rate performance (Fig. S11a†) and a specific capacity of ~80 mA h g^{-1} after 1000 cycles (Fig. S11b†) indicate the NVP used here needs more optimization, as the theoretical capacity of NVP is 117.6 mA h g^{-1}. SEM images in Fig. S11c and d† show the structural collapse of NVP after cycling. Fig. 5c shows that the full cell displays a discharge-specific capacity of ~380 mA h g^{-1} at 0.1 A g^{-1}. CV curves in Fig. S12a† show a slight polarization with the increased scan rate; GCD curves in Fig. S12b† show that the N-HC/rGO//NVP cell has a discharge plateau of ~3.4 V and good rate performance. Probably due to the structural collapse of NVP electrodes, the specific capacity of the N-HC/rGO//NVP full cell gradually decays in cycling; the capacity retention is 75% after 250 cycles. The specific energy density of the N-HC/rGO//NVP device is 287.4 W h kg^{-1} at 0.01 A g^{-1} and the specific power density is 4860 W kg^{-1} at 2.0 A g^{-1}, when being normalized to the total mass of active materials in the electrodes.

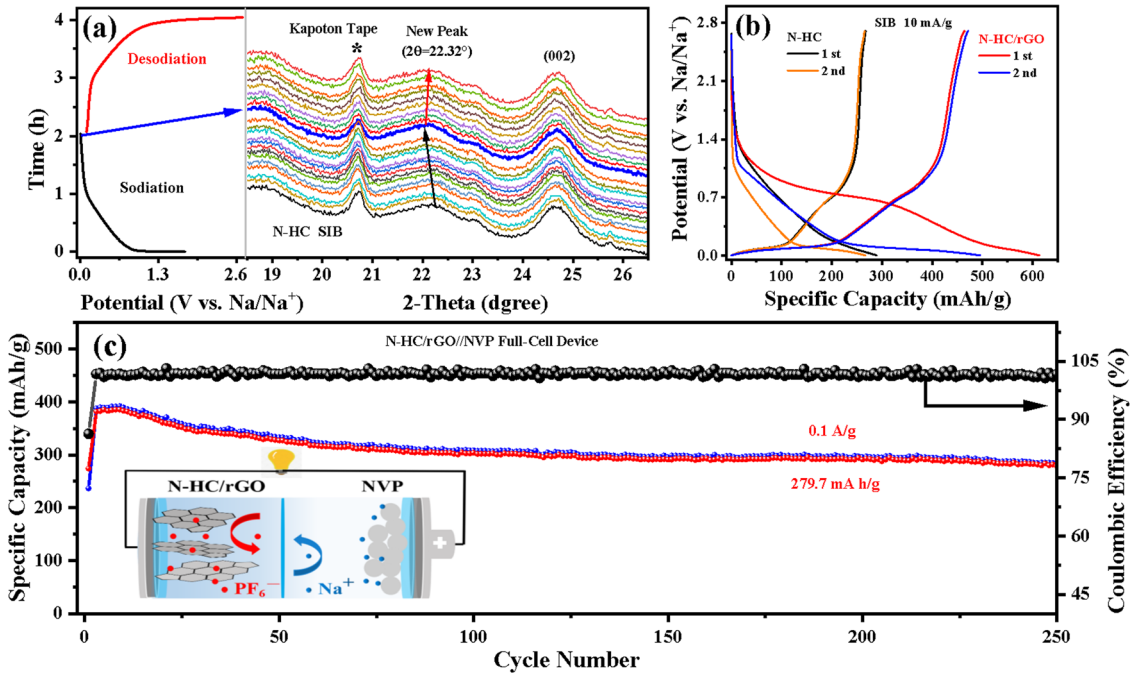

Fig. 5 (a) *In situ* XRD result of the N-HC electrode; (b) discharge curves of N-HC and N-HC/rGO electrodes at 0.01 A g^{-1} for the first two cycles; (c) cycling performance of the N-HC/rGO//NVP full cell at 0.1 A g^{-1} (inset: schematic diagram of the structure of the N-HC/rGO//NVP cell).

Conclusions

N-HC/rGO has been prepared by a dehydration reaction of sucrose with 95–98% sulfuric acid, mixing with rGO and annealing in NH_3/Ar. Compared with N-HC, N-HC/rGO contains more defects and ultra-micropores, confirmed by various characterization techniques. The electrochemical results show that N-HC/rGO has a faster Na^+ diffusion ability and good rate performance as well as cycling stability. The slope region and plateau region capacities of N-HC/rGO are higher than those of N-HC, which may be related to the existence of rGO and the abundant ultra-micropore structure of N-HC/rGO. Due to the better electrochemical performance of N-HC/rGO anodes, the energy and power densities of an assembled N-HC/rGO//NVP full cell are 287.4 W h kg^{-1} and 4860 W kg^{-1}, with a capacity retention rate of 75% after 250 cycles. Owing to the simplicity of the preparation of hard carbon by a dehydration reaction, our work may provide an industrially scalable method to produce biomass-based hard carbon anodes for SIBs.

Conflicts of interest

There are no conflicts to declare.

Acknowledgements

This work was supported by the Natural Science Foundation of China (No. 51972299, 52003265, 52273234 and 52273239), the National Key R&D Program of China (No. 2020YFA0711502) and Shandong Zero One Four Advanced Material Co., Ltd.

References

1 Z. F. Li, Y. C. Chen, Z. L. Jian, H. Jiang, J. J. Razink, W. F. Stickle, J. C. Neuefeind and X. L. Ji, *Chem. Mater.*, 2018, **30**, 4536–4542.
2 L. F. Zhao, Z. Hu, W. H. Lai, Y. Tao, J. Peng, Z. C. Miao, Y. X. Wang, S. L. Chou, H. K. Liu and S. X. Dou, *Adv. Energy Mater.*, 2021, **11**, 2002704.
3 H. U. Sverdrup, *Resour., Conserv. Recycl.*, 2016, **114**, 112–129.
4 M. A. Reddy, M. Helen, A. Groß, M. Fichtner and H. Euchner, *ACS Energy Lett.*, 2018, **3**, 2851–2857.
5 K. T. Chan, J. B. Neaton and M. L. Cohen, *Phys. Rev. B*, 2008, **77**, 235430.
6 S. Q. Li, K. Wang, G. F. Zhang, S. Li, Y. N. Xu, X. D. Zhang, X. Zhang, S. H. Zheng, X. Z. Sun and Y. W. Ma, *Adv. Funct. Mater.*, 2022, **32**, 2200796.
7 R. A. Adams, A. Varma and V. G. Pol, *Adv. Energy Mater.*, 2019, **9**, 1900550.
8 T. Gao, C. Y. Xu, R. Q. Li, R. Zhang, B. L. Wang, X. F. Jiang, M. Hu, Y. Bando, D. S. Kong, P. C. Dai and X. B. Wang, *ACS Nano*, 2019, **13**, 11901–11911.
9 X. P. Yin, Y. F. Zhao, X. Wang, X. C. Feng, Z. X. Lu, Y. Li, H. L. Long, J. Wang, J. Y. Ning and J. J. Zhang, *Small*, 2022, **18**, 2105568.
10 Y. W. Wan, N. Xiao, Z. Y. Wang, H. J. Li, M. L. Yu, Y. C. Tang, M. Y. Hao, C. Liu, Y. Zhou and J. S. Qiu, *Chem. Eng. J.*, 2018, **342**, 52–60.
11 K. F. Wang, F. Sun, H. Wang, D. Y. Wu, Y. X. Chao, J. H. Gao and G. B. Zhao, *Adv. Funct. Mater.*, 2022, **32**, 2203725.
12 M. H. Zhang, Y. Li, F. Wu, Y. Ba and C. Wu, *Nano Energy*, 2021, **82**, 105738.

13 Y. Sun, X. L. Shi, Y. L. Yang, G. Q. Suo, L. Zhang, S. Y. Lu and Z. G. Chen, *Adv. Funct. Mater.*, 2022, **32**, 2201584.
14 P. Liu, Y. M. Li, Y. S. Hu, H. Li, L. Q. Chen and X. J. Huang, *J. Mater. Chem. A*, 2016, **4**, 13046–13052.
15 N. Sun, H. Liu and B. Xu, *J. Mater. Chem. A*, 2015, **3**, 20560–20566.
16 F. Wu, M. H. Zhang, Y. Bai, X. R. Wang, R. Q. Dong and C. Wu, *ACS Appl. Mater. Interfaces*, 2019, **11**, 12554–12561.
17 M. Dahbi, M. Kiso, K. Kubota, T. Horiba, T. Chafik, K. Hida, T. Matsuyama and S. Komaba, *J. Mater. Chem. A*, 2017, **5**, 9917–9928.
18 Y. E. Zhu, L. P. Yang, X. L. Zhou, F. Li, J. P. Wei and Z. Zhou, *J. Mater. Chem. A*, 2017, **5**, 9528–9532.
19 Q. Q. Wang, X. S. Zhu, Y. H. Liu, Y. Y. Fang, X. S. Zhou and J. C. Bao, *Carbon*, 2018, **127**, 658e666.
20 Q. Li, X. S. Liu, Y. Tao, J. X. Huang, J. Zhang, C. P. Yang, Y. B. Zhang, S. W. Zhang, Y. R. Jia, Q. W. Lin, Y. X. Xiang, J. Cheng, W. Lv, F. Y. Kang, Y. Yang and Q. H. Yang, *Natl. Sci. Rev.*, 2022, **9**, nwac084.
21 J. L. Xia, D. Yan, L. P. Guo, X. L. Dong, W. C. Li and A. H. Lu, *Adv. Mater.*, 2020, 2000447.
22 Y. Youn, B. Gao, A. Kamiyama, K. Kubota, S. Komaba and Y. Tateyama, *npj Comput. Mater.*, 2021, **7**, 48.
23 A. Kamiyama, K. Kubota, D. Igarashi, Y. Youn, Y. Tateyama, H. Ando, K. Gotoh and S. Komaba, *Angew. Chem., Int. Ed.*, 2021, **60**, 5114–5120.
24 E. F. Quezada, E. D. L. Llave, E. Halac, M. Jobbágy, F. A. Viva, M. M. Bruno and H. R. Corti, *Chem. Eng. J.*, 2019, **360**, 631–644.
25 W. Cha, S. Kim, P. Selvarajan, J. M. Lee, J. M. Davidraj, S. Joseph, K. Ramadas, I. Y. Kim and A. Vinu, *Nano Energy*, 2021, **82**, 105733.
26 B. Zhang, C. M. Ghimbeu, C. Laberty, C. V. Guterl and J. M. Tarascon, *Adv. Energy Mater.*, 2016, **6**, 1501588.
27 S. Q. Zhao, Y. J. He, Z. W. Wang, X. X. Bo, S. M. Hao, Y. F. Yuan, H. L. Jin, S. Wang and Z. Q. Lin, *Adv. Energy Mater.*, 2022, **12**, 2201015.
28 M. Yuan, C. Y. Meng, A. Li, B. Cao, Y. Dong, D. Wang, X. W. Liu, X. H. Chen and H. H. Song, *Small*, 2022, 2105738.
29 Y. Wang, C. Y. Wang, Y. J. Wang, H. K. Liu and Z. G. Huang, *ACS Appl. Mater. Interfaces*, 2016, **8**, 18860–18866.
30 Z. Q. Tan, K. Ni, G. X. Chen, W. C. Zeng, Z. C. Tao, M. Ikram, Q. B. Zhang, H. J. Wang, L. T. Sun, X. J. Zhu, X. J. Wu, H. X. Ji, R. S. Ruoff and Y. W. Zhu, *Adv. Mater.*, 2017, 1603414.
31 V. Ţucureanu, A. Matei and A. M. Avram, *Crit. Rev. Anal. Chem.*, 2016, **6**, 502–520.
32 B. Wang, Y. H. Wang, Y. Y. Peng, X. Wang, N. Wang, J. Wang and J. B. Zhao, *Chem. Eng. J.*, 2018, **348**, 850–859.
33 J. M. Fei, S. Q. Zhao, X. X. Bo, F. R. Xie, G. H. Li, E. A. M. A. Ahmed, Q. C. Zhang, H. L. Jin and Z. Q. Lin, *Carbon Energy*, 2023, e333.
34 P. Lu, Y. Sun, H. F. Xiang, X. Liang and Y. Yu, *Adv. Energy Mater.*, 2018, **8**, 1702434.
35 Z. M. Jiang, S. Zhang, J. Feng, Y. T. Jiang, S. C. Liang, Q. Q. Li, M. J. Shi, M. Cao, M. Y. Zhang, T. Wei and Z. J. Fan, *J. Energy Chem.*, 2022, **73**, 35–40.
36 A. Beda, F. Rabuel, M. Morcrette, S. Knopf, P. L. Taberna, P. Simon and C. M. Ghimbeu, *J. Mater. Chem. A*, 2021, **9**, 1743–1758.
37 Q. N. Zhao, K. Q. Zhao, G. P. Ji, X. L. Guo, M. Han, J. Wen, Z. L. Ren, S. C. Zhao, Z. Gao, R. H. Wang, M. Li, K. Sun, N. Hu and C. H. Xu, *Chem. Eng. J.*, 2019, **361**, 1043–1052.
38 F. R. Xie, S. Q. Zhao, X. X. Bo, G. H. Li, J. M. Fei, E. A. M. A. Ahmed, Q. C. Zhang, H. L. Jin, S. Wang and Z. Q. Lin, *J. Mater. Chem. A*, 2023, **11**, 53–67.